

Chapter 1

Transport barrier relaxations in tokamak edge plasmas

P. Beyer
Université de Provence

1.1 Introduction

Transport barriers at the plasma edge are key elements of high confinement modes (H-modes) in fusion devices. These barriers, characterized by a local steepening of density and temperature gradients, are strongly linked to shear flows that reduce significantly turbulent heat and particle transport. During a transition from low to high confinement (L-H transition), an edge transport barrier builds up spontaneously [1, 2, 3]. A barrier can also be produced by externally driving an ExB shear flow via edge biasing techniques [4, 5, 6].

In the most promising operational regime of future reactors, the edge transport barrier is not stable but relaxes quasi-periodically. During such fast relaxation events, turbulent transport through the barrier increases strongly and the pressure inside the barrier drops. Thereafter, the barrier builds up again on a slow, collisional time scale. The basic physical mechanism underlying these relaxation oscillations is not fully understood. In particular, there is no universal explanation why the plasma, instead of remaining in a state of marginal stability, oscillates close to stability limits. Currently, transport barrier relaxations are modeled by phenomenologically constructed dynamical equations for the amplitudes of relevant modes [7, 8, 9, 10].

Here, we propose three dimensional (3D) fluid turbulence simulations and subsequent one dimensional (1D) modelling to investigate non linear barrier dynamics [11]. In the simulations, a barrier is produced by an externally imposed ExB shear flow and it is found to relax quasi-periodically in a range of ExB shear rates. This behavior persists even if the ExB flow is

frozen, i.e. turbulent flow generation is suppressed. Hence, the mechanism at work departs from previously reported explanations based on turbulent shear flow generation [12, 13]. The relaxation dynamics is found to be governed by the intermittent growth of a mode localized at the barrier center, characterized by low poloidal and toroidal wavenumbers. A one dimensional (1D) model for the dynamics of this mode is derived. An analytical study reveals that the effect of the ExB shear flow is different from a shift of the linear instability threshold. In fact, the dynamics is found to be governed by a time delay for effective velocity shear stabilization.

1.2 Model for resistive ballooning turbulence

Resistive ballooning mode (RBM) turbulence at the edge of a tokamak plasma is modeled by reduced resistive magneto-hydrodynamical (MHD) equations for the electrostatic potential ϕ and pressure p [14],

$$\frac{n_0 m_i}{B_0^2} (\partial_t + \vec{u}_E \cdot \nabla) \nabla_\perp^2 \phi = \nabla_\parallel j_\parallel - \mathbf{G}p + \frac{\mu_{i\perp 0}}{B_0^2} \nabla_\perp^4 \phi, \quad (1.1)$$

$$(\partial_t + \vec{u}_E \cdot \nabla) p = \Gamma p_0 \mathbf{G}\phi + \chi_{\parallel 0} \nabla_\parallel^2 p + \chi_{\perp 0} \nabla_\perp^2 p + S(r), \quad (1.2)$$

where the coefficients are evaluated with reference values of the density n_0 , the pressure p_0 , the magnetic field B_0 , the perpendicular collisional ion viscosity $\mu_{i\perp 0}$ and the effective parallel and perpendicular collisional heat diffusivities $\chi_{\parallel 0}$, $\chi_{\perp 0}$. The ion mass is designated by m_i and the adiabatic index is $\Gamma = \frac{5}{3}$. Equation (1.1) corresponds to the charge balance in the drift approximation involving the divergences of the polarization current, the parallel current, and the diamagnetic current, and viscous effects, respectively. Equation (1.2) corresponds to the energy balance where $S(r)$ represents an energy source located at the plasma core. The compressibility of diamagnetic current $\vec{j}_{dia} = \vec{B}/B^2 \times \nabla p$ and electric drift $\vec{u}_E = \vec{B}/B^2 \times \nabla \phi$ gives rise to curvature terms,

$$\nabla \cdot \left(\frac{\vec{B}}{B^2} \times \nabla f \right) \equiv \mathbf{G}f, \quad \text{with } f = p, \phi. \quad (1.3)$$

In this MHD model, the diamagnetic velocity is neglected with respect to the ExB velocity, and the parallel current is evaluated using a simplified electrostatic Ohm's law, $\eta_{\parallel 0} j_\parallel = -\nabla_\parallel \phi$, where $\eta_{\parallel 0}$ is a reference value of the parallel resistivity.

The magnetic field is described by

$$\vec{B} = B_\varphi \left[\hat{e}_\varphi + \frac{r}{Rq(r)} \hat{e}_\theta \right]$$

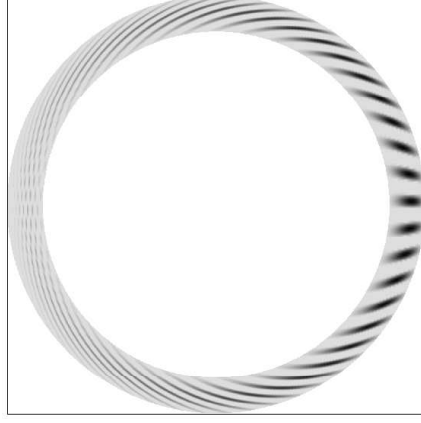


Figure 1.1. Electrostatic potential corresponding to a linear ballooning mode in the poloidal plane $\varphi = 0$.

in toroidal co-ordinates (r, θ, φ) , where R is the major radius and $q(r)$ is the safety factor. Assuming a monotonically increasing safety factor $q(r)$, the domain chosen here covers a region between $q = 2$ and $q = 3$ at the plasma edge. At the vicinity of a reference surface r_0 corresponding to $q = q_0 = 2.5$, a linear approximation of the inverse safety factor is used,

$$\frac{1}{q} = \frac{1}{q_0} - \frac{R_0}{L_s r_0} (r - r_0) .$$

Here L_s is the magnetic shear length at the reference surface.

Resistive ballooning modes are the eigenmodes of the system (1.1, 1.2), linearized with respect to the equilibrium state

$$\begin{aligned} \bar{\phi}(r) = 0, \quad \partial_r \bar{p}(r) &= -\frac{1}{\chi_\perp r} \int_{r_{min}}^r r' S(r') dr' = -\frac{1}{\chi_\perp} \Gamma_{tot}(r) \\ \rightarrow \bar{p}(r) &= -\frac{p_0}{L_p} (r - a) \quad \text{for } r \geq r_{q=2}, \end{aligned} \quad (1.4)$$

where the source $S(r)$ is radially located between r_{min} and $r_{q=2}$ such that the total energy flux $\Gamma_{tot} = (1/r) \int_{r_{min}}^r r' S(r') dr'$ is constant in the main computational domain between $r_{q=2}$ and $r_{q=3}$. Here, $L_p = \chi_\perp p_0 / \Gamma_{tot}$ is a characteristic value of the pressure gradient length and a is the outer radial boundary of the plasma. The equilibrium (1.4) is unstable if the pressure gradient $-\partial_r \bar{p}$ is larger than a critical value κ_0 . In this case, resistive ballooning modes

$$\begin{pmatrix} \tilde{\phi} \\ \tilde{p} \end{pmatrix} (r, \theta, \varphi, t) = \begin{pmatrix} \hat{\phi}_n \\ \hat{p}_n \end{pmatrix} (r, \theta) \exp(in\varphi + \gamma t),$$

characterized by the toroidal wavenumber n , have a positive growth rate γ . Fig. 1.1 shows the structure in the (r, θ) plane of such a mode for $n = 18$. The mode balloons at the low field side $\theta \approx 0$ (to the right in Fig. 1.1), where the magnetic curvature

$$\left(\frac{\vec{B}}{B} \cdot \nabla \right) \frac{\vec{B}}{B} \approx \frac{1}{R_0} \left[\sin \theta \hat{e}_\theta - \cos \theta \hat{e}_r + \mathcal{O} \left(\frac{a}{R_0} \right) \right]$$

is in the same direction as pressure gradient $(\partial_r \bar{p}) \hat{e}_r$. The mode can be decomposed into a series of Fourier modes

$$\begin{pmatrix} \hat{\phi}_n \\ \hat{p}_n \end{pmatrix} (r, \theta) = \sum_m \begin{pmatrix} \hat{\phi}_{mn} \\ \hat{p}_{mn} \end{pmatrix} (r) \exp i m \theta ,$$

where m is the poloidal mode number. Each Fourier component $(\hat{\phi}_{mn}, \hat{p}_{mn}) (r)$ has a characteristic radial width ξ_{bal} with $\xi_{bal}^2 = m_i n_0 \eta_{||0} L_s^2 / (\tau_{int} B_0^2)$. In a strongly ballooned case, i.e. if $(\hat{\phi}_n, \hat{p}_n)(r, \theta)$ is strongly localized at the low field side $\theta \approx 0$, the growth rate γ is close to the interchange growth rate $1/\tau_{int}$ with $\tau_{int}^2 = R_0 L_p / (2c_{S0}^2)$, where c_{S0} is the reference sound speed with $c_{S0}^2 = p_0 / (n_0 m_i)$. Note however, that in typical cases as the one shown in Fig. 1.1, the growth rate γ is considerably lower compared to $1/\tau_{int}$, as the mode is stabilized by its components on the high field side $\theta \approx \pi$ where the magnetic curvature is opposed to the pressure gradient.

The system (1.1, 1.2) can be normalized using the characteristic time is τ_{int} and perpendicular length ξ_{bal} ,

$$\frac{t}{\tau_{int}} \rightarrow t , \quad \frac{(r-r_0, r_0 \theta)}{\xi_{bal}} \rightarrow (x, y) , \quad \frac{R_0 \varphi}{L_s} \rightarrow z , \quad \frac{\tau_{int} \phi}{B_0 \xi_{bal}^2} \rightarrow \phi , \quad \frac{L_p p}{\xi_{bal} p_0} \rightarrow p .$$

The normalized system takes the form

$$\partial_t \nabla_\perp^2 \phi + \{ \phi, \nabla_\perp^2 \phi \} = -\nabla_\parallel^2 \phi - \mathbf{G} p + \nu \nabla_\perp^4 \phi , \quad (1.5)$$

$$\partial_t p + \{ \phi, p \} = \delta_c \mathbf{G} \phi + \chi_\parallel \nabla_\parallel^2 p + \chi_\perp \nabla_\perp^2 p + S(r) . \quad (1.6)$$

with the coefficients

$$\delta_c = 2\Gamma \frac{L_p}{R_0} , \quad \nu = \frac{\tau_{int}}{\xi_{bal}^2} \frac{\mu_{i\perp 0}}{m_i n_0} , \quad \chi_\parallel = \frac{\tau_{int}}{L_s^2} \chi_{||0} , \quad \chi_\perp = \frac{\tau_{int}}{\xi_{bal}^2} \chi_{\perp 0} .$$

As the width of the radial domain considered here is small compared to the minor radius of the reference surface, i.e. $r_{q=3} - r_{q=2} \ll r_0$, a slab geometry can be used in the numerical code leading to a simplification of the poloidal and toroidal derivatives via $r^{-1} \partial_\theta \rightarrow r_0^{-1} \partial_\theta$ and $R^{-1} \partial_\varphi \rightarrow R_0^{-1} \partial_\varphi$. The normalized operators then take the form

$$\{ \phi, \cdot \} = \partial_x \phi \partial_y - \partial_y \phi \partial_x , \quad \mathbf{G} = \sin \theta \partial_x + \cos \theta \partial_y ,$$

$$\nabla_\parallel = \partial_z + \frac{\zeta}{q} \partial_y \text{ with } \zeta = \frac{L_s r_0}{R_0 \xi_{bal}} , \quad \nabla_\perp^2 = \partial_x^2 + \partial_y^2 .$$

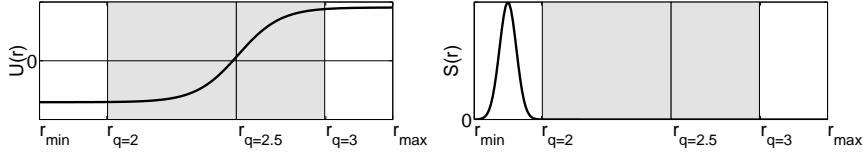


Figure 1.2. Radial profiles of the poloidal flow U (left) and the source S (right).

1.3 Formation of a transport barrier

In the present model, a transport barrier is generated by externally imposing a locally sheared poloidal ExB flow. A corresponding drive is added to the equation for the poloidal flow, i.e. the magnetic flux surface average $\langle \dots \rangle_{\theta\varphi}$ of Eq. (1.5),

$$\partial_t \bar{u}_\theta = -\frac{1}{r^2} \partial_r r^2 \langle \tilde{u}_\theta \tilde{u}_r \rangle + \nu \partial_r \frac{1}{r} \partial_r r \bar{u}_\theta - \mu (\bar{u}_\theta - U) , \quad (1.7)$$

where $\bar{u}_\theta = \langle u_\theta \rangle_{\theta\varphi}$ is the flow profile and $\tilde{u}_{r,\theta} = u_{r,\theta} - \bar{u}_{r,\theta}$ are the fluctuations of radial and poloidal velocity. The first two terms on the right hand side of (1.7) correspond to the divergences of the Reynolds stress and the viscosity stress, respectively, and the last term has been added artificially to account for the friction with an external flow U . The latter is chosen to be strongly sheared at the position r_0 , $U(r) = \omega_{E_{ext}} d \tanh[(r - r_0)/d] + U_0$, where $\omega_{E_{ext}}$ is the maximal shear, d is width of the shear layer (here $d/\xi_{bal} = 13$), and the constant U_0 is adapted such that the corresponding potential $\Phi = \int^r U dr$ vanishes at the boundaries of the radial domain. The radial profile of the flow U is plotted in Fig. 1.2 (left).

In the absence of external drive (i.e. $\mu = 0$), a poloidal flow is generated by turbulent fluctuations via Reynolds stress. This mechanism generates both, a mean component (finite time average) and a fluctuating (in time) component of the poloidal flow. The latter corresponds to the so called zonal flows [15, 16]. With increasing μ , the friction with the imposed flow gets important, the time averaged profile becomes dominated by the imposed one, and the deviations from that profile get smaller (Fig. 1.3). In the limit $\mu \rightarrow \infty$, the poloidal flow \bar{u}_θ becomes identical to the external flow U (frozen flow case). This limit is simulated in the numerical code by using a finite value μ much larger than $\nu (\xi_{bal}/d)^2$ (here $\mu = 2$) and suppressing the Reynolds stress term in Eq. (1.7).

The localized flow shear leads to a local reduction of turbulent transport [17, 18, 19]. A steepening of the pressure gradient then follows from the energy flux conservation. The latter is a consequence of the magnetic flux surface average of Eq. (1.6),

$$\partial_t \bar{p} = -\frac{1}{r} \partial_r r (\Gamma_{turb} + \Gamma_{coll}) + S , \quad (1.8)$$

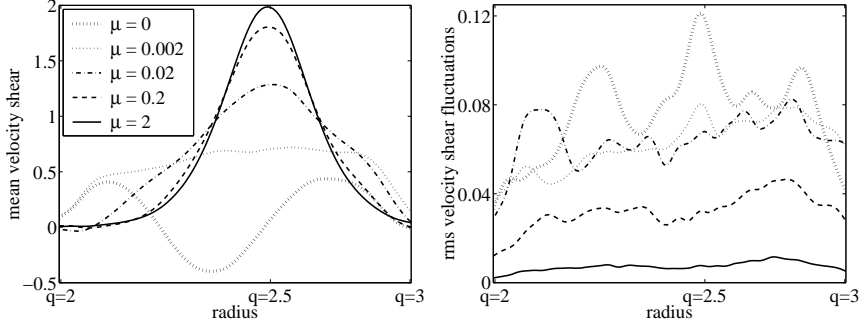


Figure 1.3. Time average profiles of the velocity shear (left) and root mean square fluctuations of these profiles (right) for different values of the friction coupling constant μ , and $\omega_{Ext} = 2$, $\Gamma_{tot} = 8$.

where $\bar{p} = \langle p \rangle_{\theta\varphi}$ corresponds to the pressure profile, $\Gamma_{turb} = \langle \tilde{p} \tilde{u}_r \rangle_{\theta\varphi}$ and $\Gamma_{coll} = -\chi_{\perp} \partial_r \bar{p}$ correspond to the turbulent and collisional radial energy fluxes, respectively. Here, $\tilde{p} = p - \bar{p}$ are the pressure fluctuations. The source S is located in an artificial (“buffer”) zone outside the main computational domain between $r_{q=2}$ and $r_{q=3}$ (see Fig. 1.2, right). It determines the total energy flux Γ_{tot} across a magnetic surface in this radial domain. In time average, according to (1.8), a local reduction of turbulent flux Γ_{turb} by an ExB shear flow leads to an increase of collisional flux Γ_{coll} , i.e. a steepening of the pressure gradient $|\partial_r \bar{p}|$. Fig. 1.4 shows radial profiles of the time averaged turbulent flux and pressure for different values of the maximal shear ω_{Ext} .

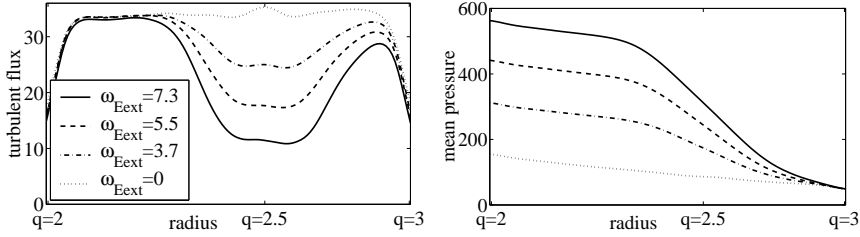


Figure 1.4. Time averaged profiles of turbulent flux and pressure for different values of the maximal shear and $\Gamma_{tot} = 36$, $\mu \rightarrow \infty$.

1.4 Appearance of relaxation oscillations

In typical RBM turbulence simulations with a transport barrier generated as described above, the barrier is not stationary but relaxes quasi-periodically. In Fig. 1.5 (left), the dynamics of the pressure gradient, the turbulent flux, and the poloidal flow shear are shown, all values are taken at the barrier center ($r = r_0$). The evolution of the pressure gradient is characterized by phases of a slow increase quasi periodically interrupted by rapid crashes. The latter correspond to relaxations of the barrier and are associated with large peaks of the turbulent flux at the barrier center as well as fluctuations of the velocity shear at the barrier position.

These relaxation oscillations are found to persist even if the poloidal flow profile is frozen. Fig. 1.5 (right) shows the corresponding results from a simulation with the same parameters as in Fig. 1.5a except that the friction coefficient is set to $\mu \rightarrow \infty$. In this case, the velocity shear profile is constant in time but intermittent flux peaks with relaxation of the barrier do appear.

When varying the maximal ExB shear ω_{Ext} and the total energy flux Γ_{tot} , two opposite trends concerning the behavior of the oscillation frequency are observed. The frequency increases with Γ_{tot} (for fixed ω_{Ext}) and decreases with ω_{Ext} (for fixed Γ_{tot}). However, in tokamaks, the ExB flow shear increases with the heating power [20]. It is found here that if this increase is faster than linear, the actual relaxation frequency decreases with power. This is illustrated in Fig. 1.6 where the dynamics of the turbulent flux is shown for two cases. With respect to case (a), the heating power

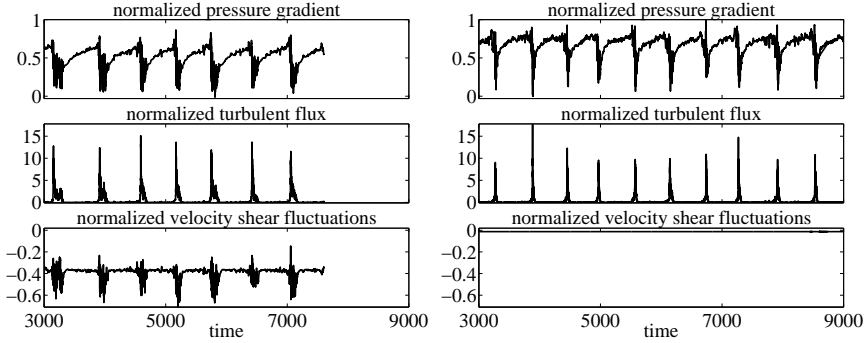


Figure 1.5. Time evolution of pressure gradient normalized to the diffusive value, $\partial_r \bar{p} / (-\Gamma_{tot} / \chi_\perp)$, turbulent flux normalized to the total incoming flux $\langle \tilde{p} \tilde{u}_r \rangle_{\theta\varphi} / \Gamma_{tot}$, and relative deviations of the poloidal flow shear from the imposed value $(\partial_r \tilde{u}_\theta - \omega_{Ext}) / \omega_{Ext}$, at the center of the barrier. Here, $\omega_{Ext} = 8$, $\Gamma_{tot} = 36$, and $\mu = 0.02$ (left) respectively $\mu \rightarrow \infty$ (right).

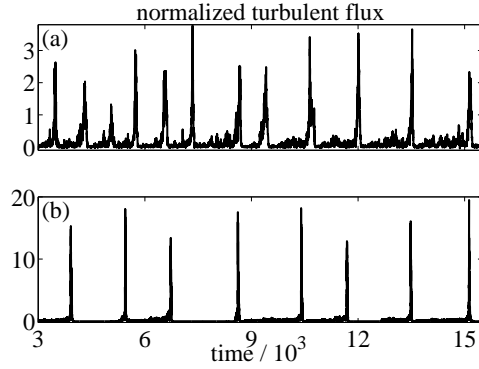


Figure 1.6. Dynamics of the turbulent flux at the barrier center for (a) $\Gamma_{tot} = 9$, $\omega_{Ext} = 2$ and (b) $\Gamma_{tot} = 36$, $\omega_{Ext} = 12$.

is four times larger and the ExB shear is six times higher in case (b). Obviously, in the latter case, the relaxation frequency is lower.

For the relaxation oscillations of transport barriers observed here, several possible mechanisms can be excluded.

- (i) As mentioned above, the relaxation mechanism at work here departs from explanations based on turbulent shear flow generation. In fact, the behavior persists even if the ExB flow is frozen, i.e. turbulent flow generation is suppressed.
- (ii) Resistive ballooning modes are global modes with a large radial extend. In general, in the simulations presented here, these modes are linearly unstable due to the components localized in the regions far from the barrier. As will be shown in the following, the components of the global modes localized at the barrier center are almost vanishing during quiescent phases but get rapidly excited during a relaxation event. This could be an effect of the toroidal coupling of the Fourier components of a global mode, leading to a pumping of the part localized at the barrier center by the unstable components localized at the shoulders. However, as can be shown in Fig. 1.7 (left), no precursor on the directly coupled neighbors at the barrier shoulder, $(m, n) = (4, 2)$ and $(6, 2)$, is observed prior to the growth of the central $(m, n) = (5, 2)$ mode. This is also true for the neighbors $(m, n) = (8, 4)$ and $(12, 4)$ of the next order central mode $(m, n) = (10, 4)$.
- (iii) The growth of a perturbation at the barrier center could in principle also be triggered by large scale transport events [21, 22, 18], as these high flux perturbations propagate radially over large distances. However, the amplitude of such bursts decreases strongly as they approach the barrier [18]. On the contrary, one observes that a relaxation event

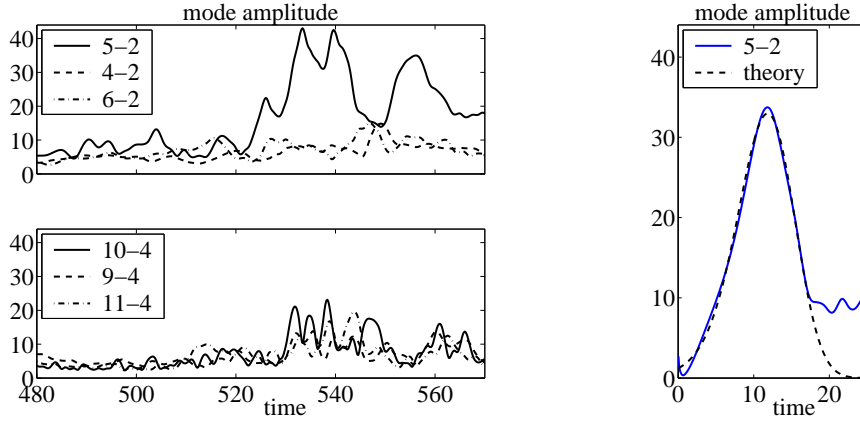


Figure 1.7. (left) Time evolution of amplitudes (of the potential) of different (m, n) modes during a flux peak. (right) Time evolution of a perturbation of the $(m, n) = (5, 2)$ mode in a restarted simulation (solid line) compared to the curve obtained from Eq. (1.12) (dashed line), as explained in the text.

leads to a flattening of the pressure gradient at the barrier center and an isolation of two regions of steep gradient on both sides. These steep gradients are then propagating radially away from the barrier center (Fig. 1.8).

- (iv) The strong velocity shear at the barrier center can in principle generate a Kelvin–Helmholtz instability. In contrast to the resistive ballooning

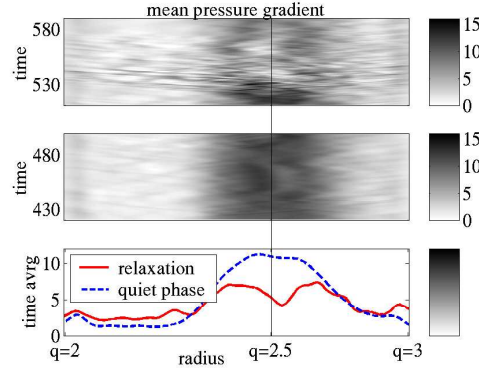


Figure 1.8. Mean pressure gradient versus radius and time during a relaxation (top) and in a quiescent phase (middle), and its time average during both phases (bottom).

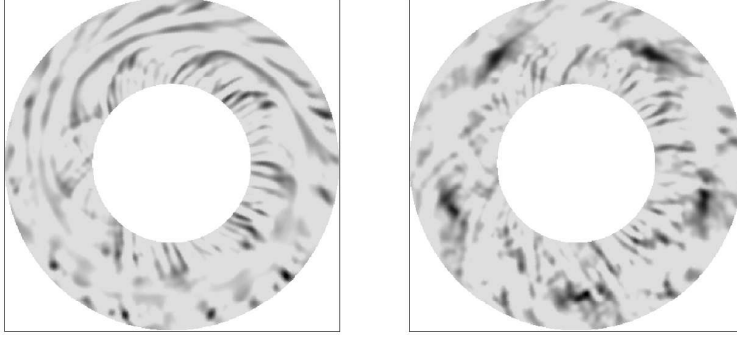


Figure 1.9. Snapshots of electric potential fluctuations in a poloidal plane in a quiescent phase (left) and during a relaxation (right). The radial co-ordinate is stretched by a factor 4 (comp. Fig. 1.1). Only positive values are shown, from zero (light gray) to the maximum (black) of 160 (left), respectively 410 (right). The relaxation is dominated by a $(m, n) = (5, 2)$ mode which is the lowest order (m, n) mode localized at the barrier position.

instability, this type of instability is independent of the magnetic curvature. However, if the magnetic curvature is suppressed artificially in our simulation, all turbulent fluctuations rapidly die out, indicating that the system is Kelvin–Helmholtz stable.

The barrier relaxation oscillations observed here are governed by the intermittent growth of a low poloidal (m) and toroidal (n) wavenumber mode localized at the barrier center. As illustrated in Fig. 1.9, a relaxation event is dominated by a $(m, n) = (5, 2)$ mode which is the lowest order (m, n) mode localized at the barrier position. This is a rather surprising result because one expects fluctuations localized at this position to be strongly stabilized by the velocity shear. However, as will be shown in the following by means of a reduced model, a transitory growth of a perturbation is possible due to the existence of a time delay for velocity shear stabilization which is an intrinsically nonlinear effect.

1.5 Low dimensional model and non-linear short-term dynamics of shear flow stabilization

A 1D model reproducing the dynamics of barrier relaxations is constructed by decomposing the pressure into the profile $\bar{p}(r, t)$ and a perturbation $\tilde{p}(r, t)e^{im\theta - in\varphi}$ localized at the barrier center, i.e. $m/n = 2.5$. In order to obtain a simplified model involving only two fields, potential fluctuations are supposed to follow pressure fluctuations via the relation $\tilde{\phi} = ik_\theta / (\gamma_0 k_\perp^2) \tilde{p}$.

The latter is obtained from balancing the two terms governing the ballooning instability in Eq. (1.1), i.e. the time derivative and the curvature term. Here, γ_0 is the linear growth rate in the case of a constant pressure gradient, $\partial_r \bar{p} = -1$, and in the absence of mean velocity, magnetic shear and dissipation. $k_\theta = m/r_0$ and k_\perp are respectively, the poloidal and perpendicular wavevectors of the corresponding mode, and a cylindrical curvature $\mathbf{G} \rightarrow r^{-1} \partial_\theta$ has been assumed. Supposing further a uniformly sheared poloidal flow, $\bar{u}_\theta = \omega_E(r - r_0)$, projections of the pressure equation (1.2) on the profile and the perturbation, respectively, lead to

$$\partial_t \bar{p} = -2\gamma_0 \partial_x |\bar{p}|^2 + \chi_\perp \partial_x^2 \bar{p} + S, \quad (1.9)$$

$$\partial_t \tilde{p} = \gamma_0 (-\partial_x \bar{p} - \kappa_0) \tilde{p} - i\omega'_E x \tilde{p} - \chi'_\parallel x^2 \tilde{p} + \chi_\perp \partial_x^2 \tilde{p}. \quad (1.10)$$

with $x = r - r_0$, $\kappa_0 = k_\theta^2 \chi_\perp / \gamma_0$, $\omega'_E = k_\theta \omega_E$, and $\chi'_\parallel = k_\theta^2 \chi_\parallel$. The system (1.9, 1.10) reproduces barrier relaxation oscillations for finite values of ω'_E (Fig. 1.10). Note that for a fixed pressure gradient $\partial_x \bar{p} = -\kappa$, Eq. (1.10) is linear and the growth rate for the most unstable radial mode is given by

$$\gamma = \gamma_0 (\kappa - \kappa_0) - \sqrt{\chi_\perp \chi'_\parallel} - \frac{\omega'^2_E}{4\chi'_\parallel}. \quad (1.11)$$

This implies that for large enough flow shear ω'_E , linear modes are completely stabilized. However, the dynamics of these modes describes only the long-term behavior of the system, i.e. an asymptotic decay of the fluctuations for sufficiently large flow shear. For the short-term dynamics, a description in terms of linear modes is not appropriate. Indeed, if the advection with the sheared flow in Eq. (1.10) is replaced by a shift of the linear instability threshold, the modified system does always evolve to a stable fixed point. In order to obtain relaxation oscillations with such a model, one has to introduce phenomenologically further elements such as a Heaviside function multiplying the instability term [10].

In fact, the short-term dynamics in the model (1.9, 1.10) is better described by the evolution of an initial pulse $\tilde{p}(x, t=0) = \hat{p}\delta(x)$, infinitely localized at $x = 0$, that can be calculated analytically from Eq. (1.10) for a given pressure gradient $-\partial_x \bar{p} = \kappa$ and when neglecting the χ_\parallel term. The solution takes the form

$$\tilde{p} = \frac{\hat{p}}{\sqrt{4\pi\chi_\perp t}} \exp\left(-\frac{x^2}{4\chi_\perp t} - \frac{i\omega'_E x}{2}t + \gamma'_0 t - \frac{t^3}{3\tau_D^3}\right), \quad (1.12)$$

where $\gamma'_0 = \gamma_0 (\kappa - \kappa_0)$ and $\tau_D = (\frac{1}{4}\chi_\perp \omega'^2_E)^{-1/3}$. Note that for $\omega'_E = \gamma'_0 = 0$, the usual solution of the diffusion equation is recovered. The expression (1.12) describes an initial transient growth of the perturbation for $\gamma'^{-1}_0 < t < (\tau_D^3 \gamma'_0)^{1/2}$ before the cubic term in the exponential dominates the linear

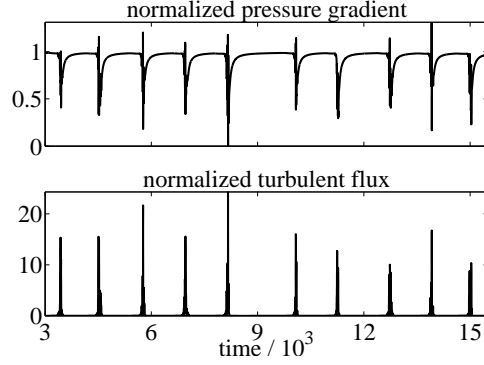


Figure 1.10. Time evolution of pressure gradient $[\partial_r \bar{p} / (-\Gamma_{tot} / \chi_\perp)]$ and turbulent flux $(2\gamma_0 |\tilde{p}|^2 / \Gamma_{tot})$ at the barrier center obtained from the 1D model (1.9, 1.10). Parameters are the same as in the 3D model and $k_\theta = 0.05$, $\gamma_0 = 0.8$, $\omega_E = 1.1$, $\Gamma_{tot} = 1.4$.

term, leading to a stabilization. The characteristic time τ_D for the transient growth is large for small values of the perpendicular diffusivity χ_\perp (close to the collisional value at the barrier center) and low poloidal wave numbers m .

From this analysis, the mechanism for relaxation oscillations is as follows. During a quiescent phase, the pressure gradient increases slowly on a collisional time scale. When it crosses the linear instability threshold, fluctuations set in and the associated anomalous flux keeps the pressure gradient close to the threshold, which tends to saturate the fluctuations. However, the latter trigger the nonlinear mechanism described above, leading to a growth of the mode during a characteristic time of the order of τ_D , even though the pressure gradient drops well below the linear stability threshold due to the large anomalous flux. For the mode shown in Fig. 1.9 (right) we have $\tau_D = 8.7$ in normalized units (with $\omega_E = 5.5$) which agrees well with the temporal width of a flux peak. The transient growth of the $(m, n) = (5, 2)$ mode is reproduced [Fig. 1.7 (right)] when restarting the simulation, initializing the $(5, 2)$ mode with a perturbation and all other (m, n) modes with noise, and keeping the pressure and velocity profiles obtained from the simulation shown in Fig. 1.7 (left) just before a relaxation. Moreover, this short term dynamics of the central mode is well described by Eq. (1.12), as can be seen from the dashed curve in Fig. 1.7 (right) that corresponds to $\tilde{p} = p_1 \exp[\gamma_0 t - t^3 / (3\tau_D^3)]$ with $p_1 = 1.2$, $\gamma_0 = 0.42$, and $\tau_D = 10$.

Note that well pronounced relaxation oscillations are found for values of ω'_E such that the linear growth rate (1.11) for the diffusive pressure gradient $\kappa_{diff} = \Gamma_{tot} / \chi_\perp$ is only slightly above the instability threshold. In

this case, the recovery phase of the profile between two relaxations is long compared to τ_D . In agreement with this picture, we find that a slight increase of the value of ω'_E leads to a completely stable situation without any fluctuations. This is also consistent with the fact that the frequency of relaxation oscillations decreases with the velocity shear ω_E , as observed in the 3D simulations.

1.6 Conclusions

In conclusion, 3D turbulence simulations with imposed ExB shear flow show the formation of a transport barrier and the appearance of relaxation oscillations. The analysis of these simulations reveals that this dynamics is governed by an effective time delay in the stabilization by the shear flow. This is confirmed by a reduced 1D model. The ExB flow shear in tokamaks increases with heating power. It is found here that if this increase is faster than linear, the relaxation frequency decreases with power. These properties, onset of a transport barrier, relaxation oscillations associated to resistive ballooning modes, and the oscillation frequency that decreases with power, are reminiscent of so-called type III edge localized mode (ELM) dynamics in tokamak edge transport barriers [23].

- [1] F. Wagner, G. Becker, K. Behringer, et al., *Phys. Rev. Lett.* **49**, 1408 (1982).
- [2] R. J. Groebner, *Phys. Fluids B* **5**, 2343 (1993).
- [3] K. H. Burrell, *Phys. Plasmas* **4**, 1499 (1997).
- [4] R. J. Taylor, M. L. Brown, B. D. Fried, et al., *Phys. Rev. Lett.* **63**, 2365 (1989).
- [5] R.R. Weynants, G. van Oost, G. Bertschinger, et al., *Nucl. Fusion* **32**, 837 (1992).
- [6] J. Cornelis, R. Sporken, G. van Oost, et al., *Nucl. Fusion* **34**, 171 (1994).
- [7] S.-I. Itoh, K. Itoh, A. Fukuyama et al., *Phys. Rev. Lett.* **67**, 2485 (1991).
- [8] V. B. Lebedev, P. H. Diamond, I. Gruzina et al., *Phys. Plasmas* **2**, 3345 (1995).
- [9] S. C. Cowley, H. Wilson, O. Hurricane et al., *Plasma Phys. Contr. Fusion* **45**, A31 (2003).
- [10] J.-S. Lönnroth, V. Parail, C. Figarella et al., *Plasma Phys. Contr. Fusion* **46**, A249 (2004).
- [11] P. Beyer, S. Benkadda, G. Fuhr-Chaudier et al., *Phys. Rev. Lett.* **94**, 105001 (2005).
- [12] H. Sugama, W. Horton, *Plasma Phys. Contr. Fusion* **37**, 345 (1995).
- [13] R. J. Colchin, M. J. Schaffer, B. A. Carreras et al., *Phys. Rev. Lett.* **88**, 255002 (2002).
- [14] P. Beyer, X. Garbet, S. Benkadda et al., *Plasma Phys. Contr. Fusion* **44**, 2167 (2002).
- [15] Z. Lin, T. S. Hahm, W. W. Lee et al., *Phys. Rev. Lett.* **83**, 3645 (1999).
- [16] P. H. Diamond et al., *Plasma Phys. Contr. Nucl. Fusion Res.* (IAEA, Vienna, 1998).

- [17] T. S. Hahm, K. H. Burrell, *Phys. Plasmas* **2**, 1648 (1995).
- [18] P. Beyer, S. Benkadda, X. Garbet, et al., *Phys. Rev. Lett.* **85** 4892 (2000).
- [19] C. F. Figarella, S. Benkadda, P. Beyer et al., *Phys. Rev. Lett.* **90**, 015002 (2003).
- [20] B. A. Carreras, D. Newman, P. H. Diamond et al., *Phys. Plasmas* **1**, 4014.
- [21] Y. Sarazin, Ph. Ghendrih, *Phys. Plasmas* **5**, 4214 (1998).
- [22] X. Garbet, Y. Sarazin, P. Beyer, et al., *Nucl. Fusion* **39**, 2063 (1999).
- [23] J. Connor, *Plasma Phys. Contr. Fusion* **40**, 531 (1998).